



Disconnection description of triple-junction motion

Spencer L. Thomas^a, Chaozhen Wei^{b,c}, Jian Han^a, Yang Xiang^b, and David J. Srolovitz^{a,d,e,1}

^aDepartment of Materials Science and Engineering, University of Pennsylvania, Philadelphia, PA 19104-6272; ^bDepartment of Mathematics, The Hong Kong University of Science and Technology, Kowloon, Hong Kong Special Administrative Region, People's Republic of China; ^cInstitute for Advanced Study, The Hong Kong University of Science and Technology, Kowloon, Hong Kong Special Administrative Region, People's Republic of China; ^dDepartment of Mechanical Engineering and Applied Mechanics, University of Pennsylvania, Philadelphia, PA 19104-6272; and ^eDepartment of Materials Science and Engineering, City University of Hong Kong, Hong Kong Special Administrative Region, People's Republic of China

Edited by Pablo G. Debenedetti, Princeton University, Princeton, NJ, and approved March 22, 2019 (received for review December 6, 2018)

Grain boundary (GB) migration in polycrystalline materials necessarily implies the concurrent motion of triple junctions (TJs), the lines along which three GBs meet. Today, we understand that GB migration occurs through the motion of disconnections in the GB plane (line defects with both step and dislocation character). We present evidence from molecular dynamics grain growth simulations and idealized microstructures that demonstrates that TJ motion and GB migration are coupled through disconnection dynamics. Based on these results, we develop a theory of coupled GB/TJ migration and use it to develop a physically based, disconnection mechanism-specific continuum model of microstructure evolution. The continuum approach provides a means of reducing the complexity of the discrete disconnection picture to extract the features of disconnection dynamics that are important for microstructure evolution. We implement this model in a numerical, continuum simulation and demonstrate that it is capable of reproducing the molecular dynamics (MD) simulation results.

materials science | metals | microstructure evolution | grain boundary migration | molecular dynamics

Grain growth has long been described as motion by mean curvature (i.e., curvature flow) (1–3); grain boundaries (GBs) migrate toward their center of curvature, reducing the total GB area and energy. Triple junctions (TJs) (lines along which three GBs meet), in turn, migrate to balance the surface tensions (and torques) exerted by the constituent GBs (4, 5), leading to a set of equilibrium dihedral angles. As GBs migrate, the TJs migrate to maintain these angles; the whole microstructure evolves via this tandem motion. While extensions exist that account for GB anisotropy (6–12), this has been the conceptual core of grain growth theory over the past half century. This theory rests on the assumption that TJs can migrate much faster than GBs (13–15). However, substantial experimental (13, 16, 17) and atomistic simulation (18) evidence demonstrates that this is often not true. Finite TJ mobility causes TJ drag, which leads to dynamic TJ dihedral angles that differ from their thermodynamic values (14, 15, 18–20). When the grain size is sufficiently small, grain growth is controlled by TJ drag rather than curvature flow (13, 14, 20–22). While mechanistic models of GB migration have gained prominence (23–28), particularly in the past decade (29–39), mechanistic models for TJ migration are only just being established (40).

Shear can drive the migration of many grain boundaries. Conversely, migrating GBs often induce shears as they migrate. Each GB is characterized by a temperature-dependent shear-coupling factor $\beta = \dot{B}/\dot{H}$, where \dot{H} is the GB velocity and \dot{B} is the shear velocity (30). This was first observed by Li et al. (41) and Bainbridge et al. (42). Shear coupling in high-angle GBs has been reported in experiments (28, 32, 43–45), ab initio calculations (46–49), and atomistic simulations (50–54). Recent theoretical predictions (33, 35–37) and transmission electron microscopy (TEM) observations (55, 56) connect shear coupling to the motion of line defects/disconnections; disconnections are characterized by both a step height h_i and Burgers vector

\mathbf{b}_i (25, 27, 57–61). This step-mediated migration mechanism was first proposed by Bollmann (62), Ashby (63), and Hirth and Balluffi (24). For each GB, there is an infinite set of possible disconnection modes $\{\mathbf{b}_i, h_i\}$ determined by the crystal structure and the relative orientations of the grains meeting at the GB (64). The ratio between the GB migration velocity v_{\perp} and shear displacement rate (across the GB) v_{\parallel} , $\beta = v_{\parallel}/v_{\perp}$, can be related to the ratio $\beta_i = \mathbf{b}_i/h_i$ for disconnection-mode i (while \mathbf{b}_i is a vector quantity, it is generally parallel to a symmetric tilt inclination of the GB; it is often used interchangeably with the scalar quantity b_i , where sign indicates direction).

The effective β and GB mobility represent thermal averages over the available disconnection modes (34, 36, 38, 55, 65). Shear coupling tends to vanish at high temperature (i.e., grain boundary sliding or migration without shear); this is associated with the nucleation and migration of multiple disconnection types with different signs of β_i .

Just as GBs migrate via the nucleation and migration of disconnections, TJ migration is also associated with disconnection motion, i.e., the flux of disconnections into/out of the TJ along their constituent GBs. The finite step height and Burgers vector of these disconnections constrain TJ motion. A TJ can migrate only such that all three GBs remain connected at the TJ; this leads to a zero displacement incompleteness condition associated with the flux of steps (40, 66). Since disconnections also carry Burgers vectors, the flux of disconnections into/out of TJs can lead to Burgers vector accumulation (Burgers vector

Significance

Many materials of industrial and scientific interest (including metals and ceramics) are polycrystalline. The defect microstructure of these materials has a profound impact on their properties and utility. Microstructure engineering yields materials with greatly enhanced qualities, but the microstructure typically evolves over time via the motion of grain boundaries and triple junctions. One must understand and guide this evolution to produce reliable enhanced materials. Much has been discovered in recent decades regarding the motion of grain boundaries—less so regarding triple junctions. This work presents observations of triple-junction migration from atomistic simulations, explains these observations by extending recent developments in grain boundary theory to triple junctions, and presents a continuum model of triple-junction migration based on this theory.

Author contributions: S.L.T., J.H., and D.J.S. designed research; S.L.T., C.W., J.H., Y.X., and D.J.S. performed research; C.W. and Y.X. contributed new reagents/analytic tools; S.L.T., C.W., J.H., Y.X., and D.J.S. analyzed data; and S.L.T. and D.J.S. wrote the paper.

The authors declare no conflict of interest.

This article is a PNAS Direct Submission.

Published under the PNAS license.

¹To whom correspondence should be addressed. Email: srol@seas.upenn.edu.

This article contains supporting information online at www.pnas.org/lookup/suppl/doi:10.1073/pnas.1820789116/-DCSupplemental.

Published online April 15, 2019.

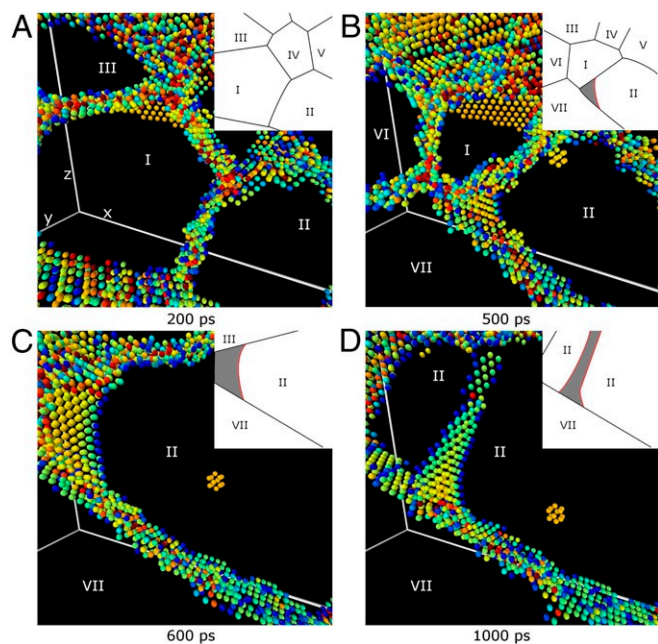


Fig. 2. (A–D) The 5-nm-thick cross-sections from the MD polycrystal grain growth simulation shown in Fig. 1. FCC atoms (common neighbor analysis) are not shown and the remaining atoms are colored by centrosymmetry (83). The white lines depict the simulation cell boundaries. A–D, Insets are schematic representations of the microstructure (lines are GBs; roman numerals label grains)—a pair of partial dislocations (red) separated by a stacking fault (gray) is emitted from the I/III/IV TJ that migrates up and left.

from triple junctions has also been observed experimentally (67–70). Fig. 3 shows a migrating TJ leaving behind a set of closely spaced coherent twin boundaries. As with dislocations, nearly all of the twin boundaries that did not form during the initial relaxation of the GB network formed at triple junctions during grain growth. While twinning at TJs has been proposed as a mechanism for relaxing the total energy of the GB network (74), this does not explain the successive twinning during TJ motion/grain growth observed here. It is possible, however, that twin formation may relax internal stresses [as has already been suggested to explain successive deformation twinning in the vicinity of two GBs (86)]. This begs the question, What is the origin of these internal stresses?

TJ Migration Simulations

While the MD simulations of polycrystal grain growth faithfully represent TJs and GBs as they occur in the “wild” (i.e., in a polycrystal) without the need for all of the simplifying assumptions made in grain growth theories, the complexity of the polycrystalline microstructure confounds attempts to draw precise conclusions on how TJs move. We therefore perform two sets of MD simulations in more “tame” circumstances, where TJ kinetics may be more directly probed. The first one employs a tricrystal configuration, where the microstructure relaxes from an initial, nonequilibrium geometry toward equilibrium via coupled GB and TJ migration. The second set consists of a single, initially elongated grain spanning an otherwise flat GB; for a sufficiently elongated grain this will lead to steady-state TJ migration as long as the grain width is small compared with the TJ separation (according to a curvature flow model, Eq. 1). Similar geometries were used both in experiment (17, 19) and in atomistic simulations studies of the TJ drag effect (18, 87).

In the tricrystal simulations (Fig. 4), a cylindrical simulation cell (radius $R \approx 37.5$ nm) was divided into three grains, all shar-

ing a common [210] axis parallel to the TJ line which initially lies along the cylinder axis. The vertical GB, labeled 1, is a symmetric tilt GB ($\Sigma 9$, 96.38° misorientation). The other GBs, labeled 2 and 3, are also initially symmetric tilt GBs ($\Sigma 15$, $\pm 48.19^\circ$ misorientation)—see *SI Appendix, Note 3* for more detail. The ends of GBs 1, 2, and 3 were fixed on the perimeter of the cylindrical simulation cell by fixing the atomic positions in a thin shell along the circumference (the effect of pinning the ends is discussed in *SI Appendix, Note 2*). The system inside this shell then evolves via molecular dynamics in an NPT ensemble with zero stress along the axial direction. Multiple simulations were performed, varying both simulation temperature (at 800 K, 1,000 K, and 1,200 K) and pinning-point (2 and 3) locations.

Triple-junction dihedral angles are difficult to measure reliably in an MD simulation because of the discreteness of the lattice and thermal fluctuations. Therefore, we directly measure an effect of dihedral/TJ angle $\phi(t)$ and TJ location $z(t)$ from the triangle formed by the pinning points 2 and 3 and the TJ, as shown schematically in Fig. 4, *Upper Right*. The triple-junction angle $\phi(t)$ and the TJ position $z(t) \leq 0$ are related through

$$\tan\left(\frac{\phi(t)}{2}\right) = \frac{\sin\left(\frac{\phi(0)}{2}\right)}{\cos\left(\frac{\phi(0)}{2}\right) + \frac{z(t)}{R}}, \quad [3]$$

where $\phi(0)$ is the initial TJ angle [its initial position is along the cylinder axis, $z(0) = 0$] that also describes the location of the pinning points. If the GBs are nearly flat as they migrate (Fig. 4), then ϕ is approximately equal to the dihedral angle $\Theta^{(1)}$ [in equilibrium $\phi(\infty) = \Theta^{(1)}$].

The time evolution of ϕ is shown in Fig. 5A at the highest temperature, 1,200 K. At this temperature, the TJ migrates slower and slower as time passes, asymptotic at late time to $\phi(\infty) \approx 100^\circ$ (achieved during the 12-ns simulations) for all initial-angle TJ angles (i.e., location of the pinning points 2 and 3). The fact that the TJs in all simulations at this temperature converge to the same angle suggests that the TJ reaches equilibrium,

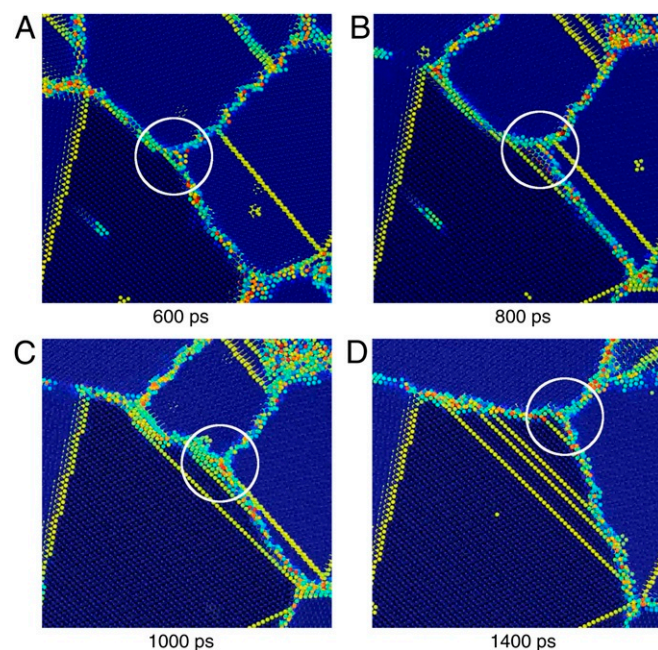


Fig. 3. Cross-section from a polycrystalline MD grain growth simulation, colored by centrosymmetry. (A–D) A TJ (circled) migrates up and to the right, leaving behind multiple, parallel, coherent twin boundaries (thin yellow lines of atoms).

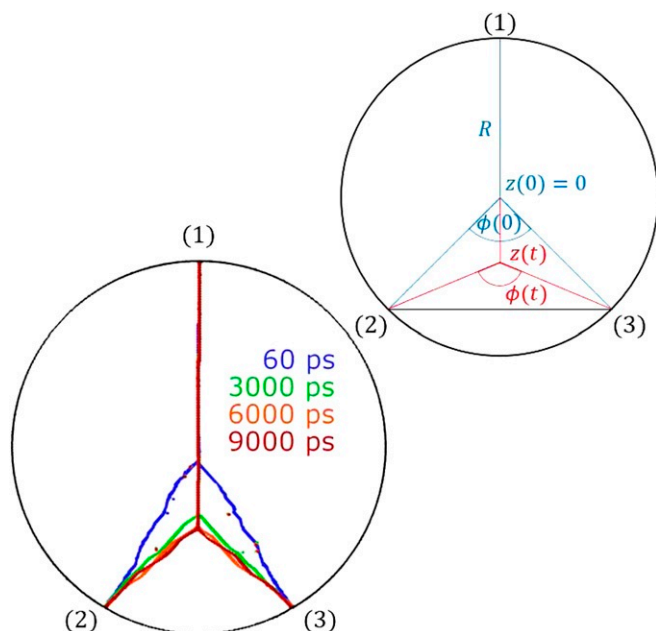


Fig. 4. (Lower Left) Time series of a 1,200-K tricrystal MD simulation. The FCC atoms were removed and the remaining atoms were colored by time after initial relaxation. The atoms on the surface of the cylindrical simulation cell (black) were held fixed, pinning GBs 1 and 2 at the simulation cell perimeter. This simulation is represented by the red open circles in Fig. 5. The GBs and TJs migrate such that the TJ is at position $z(t)$. Replacing the actual GB profile with straight lines from points 2 and 3 to the TJ, the TJ angle $\phi(t)$ is related to the TJ position $z(t)$ as in Eq. 3, as indicated in the schematic (Upper Right).

$\phi(\infty) = \Theta^{(1)}$. On the other hand, at the intermediate (1,000 K) and lowest (800 K) simulation temperatures, the TJ moves slowly and continues to move at the end of the 12-ns simulation time. This suggests that equilibrium has yet to be achieved. This is supported by the observation that simulations starting with different initial TJ angles $\phi(0)$ do not achieve the same values by the end of the simulation time when $T < 1,200$ K. Fig. 5 B and C shows the details of migration during the initial nanosecond for several simulations. At the very earliest times, the TJs all move at comparable rates for all temperatures; at low temperatures, the TJ subsequently stagnates to the velocity seen at long times.

Fig. 6A shows the higher-resolution image of the region around the TJ from the 800 K, $\phi(0) = 134^\circ$ simulation at 0.2 ns and 5 ns. In this case, the TJ is moving very slowly. In Fig. 6A we see that the TJ is not symmetric and that a disconnection that is initially present on the GB in the lower left moves into the TJ, shifts the GB in the lower left downward, and displaces the TJ (toward the right). This is a unit step of the disconnection-mediated TJ migration. Fig. 6B shows the shear stress field near the TJ for the same two configurations. The very fine-scale features in Fig. 6B1 are associated with the structure of the GB itself. Note that when the disconnection in Fig. 6B1 moves into the TJ in Fig. 6B2, the stress field around the TJ changes dramatically on a large scale compared with the stress features of the GBs themselves. Analysis of the stress field around the TJ after disconnection absorption shows that this stress is associated with the net addition of the disconnection Burgers vector. This observation suggests that disconnection flux into the TJ both conserves Burgers vector and builds the TJ stress field.

We now turn to the motion of the elongated grain embedded into the bicrystal simulations. Fig. 7A shows a time series of one

of the embedded-loop simulations. These simulations are reminiscent of simulations performed by Upmanyu et al. (18, 87); however, unlike those simulations, these are fully 3D, are performed over a range of temperatures, and focus on a high-angle tilt GB in place of a low-angle GB for GB⁽¹⁾. In these simulations, periodic boundary conditions are applied in the y and z directions with free surfaces in the x direction. Over the course of the simulation, GBs 2 and 3 facet; the system remains in this state for an extended period. Eventually, the upper TJs suddenly and very rapidly migrate, annihilating the central grain. Repeating this simulation under exactly the same conditions (except different initial velocities) and for a wide range of temperatures demonstrates that this result is repeatable; see Fig. 7B where we plot the y coordinate of the upper TJ vs. the logarithm of the time. At the highest temperature (1,200 K), the waiting period is very short (0.3 ns) and grows quickly with decreasing temperature. In most simulations, once the upper TJ starts to migrate, it does so smoothly. In all cases, GBs 2 and 3 strongly facet and these faceted GBs do not migrate inward before TJ migration. We do not report the results for the few cases (6 of 40) in which either the lower TJ migrates first or both begin migrating simultaneously.

The motion of the TJ appears to depend on two timescales—one that characterizes the wait or stagnation time for the TJ to start moving and the other associated with the finite TJ migration velocity. Once the TJ begins migrating, the grain shrinks and the capillarity-driving force for migration increases (hence the TJ accelerates). At this point, the evolution becomes complex, consisting of simultaneous inward motion of the two TJs as well as changes in the facet sizes of the vertical GBs. We can quantify the time before the TJ begins migrating by a wait time τ ; we measure this from the time of the initial relaxation (faceting) to the time the TJ passes a particular point (i.e., the dotted line in Fig. 7B). τ was averaged over eight simulations at the same temperature. Fig. 7C shows an Arrhenius plot of τ vs. inverse temperature ($\tau_0 = 1$ ns). The fact that these data fall on a straight line demonstrates that the wait time for the initiation of TJ migration is thermally activated with an activation barrier of approximately 0.57 eV. Since the timescale associated with the actual TJ migration is short, this estimate is insensitive to the choice of the dashed line in Fig. 7B. The magnitude of this activation barrier is comparable to nudged elastic band (NEB) calculations for disconnection nucleation (36, 88). However, this agreement should be viewed with caution since these NEB calculations were performed for GBs other than those in our simulations and they were based on zero temperature energy surfaces (no entropy effects). Nonetheless, the agreement suggests (rather than proves) that the “liberation” of the previously stagnant TJ may be associated with disconnection nucleation on one of the GBs. The wait time for TJ motion is long compared with the migration time, suggesting that the initial disconnection nucleation may be slow compared with subsequent nucleation events. Perhaps this indicates a change in disconnection nucleation (e.g., heterogeneous rather than homogeneous).

The polycrystal simulations and TJ kinetics simulations yield a number of important observations. Triple junctions are the source of many defects that form during grain growth, among them dislocations and twins. Some triple junctions migrate much more readily than others. At high temperatures, TJs appear to migrate consistent with conventional theory (smoothly until they reach a consistent set of equilibrium dihedral angles). At low temperature, TJs may migrate a short distance and stagnate. This stagnation may be associated with the stresses generated by disconnection adsorption. Stagnated TJs can migrate, but the process that facilitates this migration appears to be thermally activated and much slower than the initial and subsequent TJ migration. We now examine these observations in light of a disconnection dynamics approach.

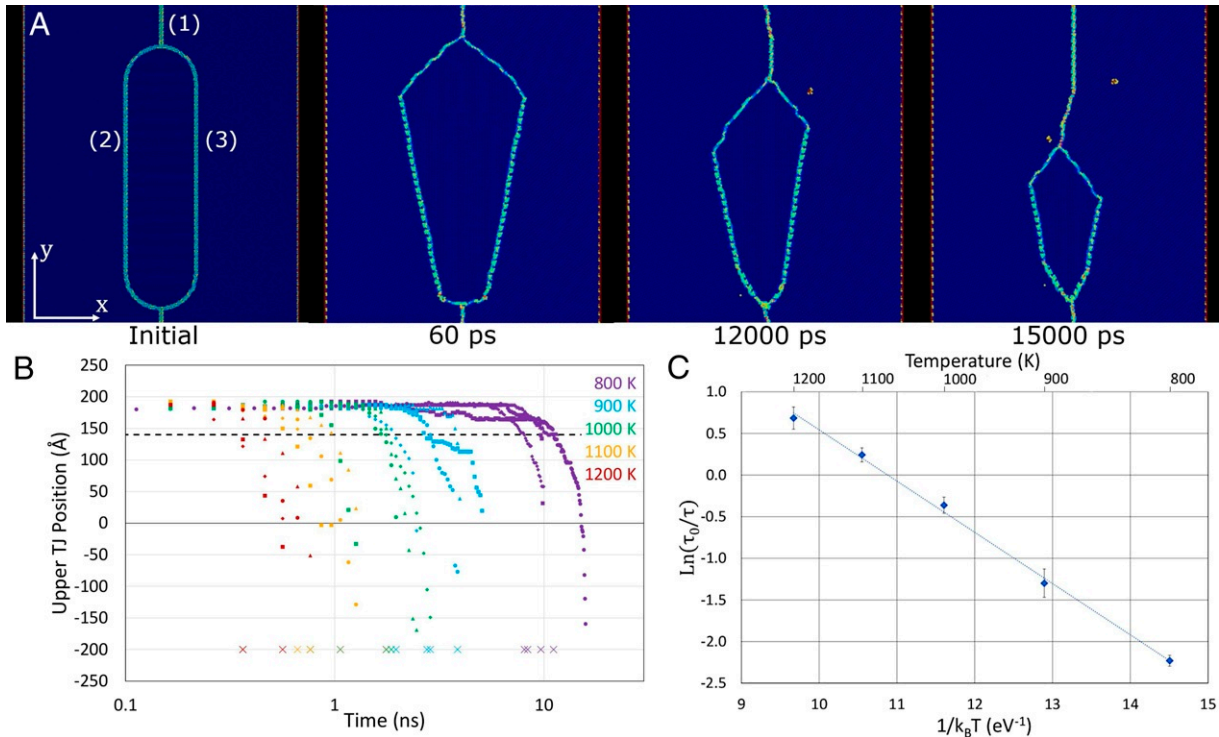


Fig. 7. (A) Time series of an embedded loop simulation at 800 K. After the GBs facet, the microstructure is stationary for a period and then suddenly migrates rapidly. (B) TJ position vs. time for multiple simulations at different temperatures. Series with the same color are from simulations performed at the same temperature. The Xs at the bottom show the time τ that the TJ crossed the dotted line at the corresponding temperature. (C) Arrhenius plot of $\ln \tau_0/\tau$, where $\tau_0 = 1$ ns and τ is the time after initial relaxation that the TJ passes the dotted line in B, averaged over six simulations at each temperature. This plot gives an activation energy of $0.57 \text{ eV} \pm 0.02 \text{ eV}$.

content annihilates, moving the TJ. However, the disconnection Burgers vectors do not simply vanish; the total Burgers vector is conserved. This implies that in all but very special cases, the net result of disconnection-mediated TJ motion is the accumulation of Burgers vector at the TJ. However, as the residual Burgers vectors accumulate, the resulting stress fields will repel subsequent disconnections, stagnating TJ migration. Long-distance TJ migration is possible only if there is no accumulation of stress, implying an additional Burgers vector cancellation condition

$$\sum_{i=1}^3 J^{(i)} \mathbf{b}^{(i)} = 0. \quad [6]$$

This equation represents three conditions on the three variables $J^{(i)}$. Combined with the zero displacement incompleteness condition, the system is overdetermined—there are more equations than variables and valid solutions exist only for (very) special cases (e.g., pure step disconnections, disconnections with parallel Burgers vectors, etc.). However, since experiments and MD simulations show that triple junctions do migrate long distances, something else must happen; several mechanisms can facilitate triple-junction migration, either by adding degrees of freedom or by relaxing the resulting stresses.

Bicrystallography permits a discrete, infinite set of disconnection modes to any GBs. While GB migration favors disconnection modes with low nucleation/migration barriers, each disconnection mode responds differently to driving forces on the boundary. A GB can switch to secondary modes under a given set of driving forces [e.g., when there are competing driving forces for migration (65)]. Secondary-mode nucleation is associated with GB sliding as well as GB migration without shear coupling,

but it may also facilitate TJ migration. If $\text{GB}^{(i)}$ is populated with N_i types of disconnections, then Eq. 6 becomes

$$\sum_{i=1}^3 \sum_{j=1}^{N_i} J_j^{(i)} \mathbf{b}_j^{(i)} = 0, \quad [7]$$

where the summation on j represents all disconnection modes of each GB. This modification adds many degrees of freedom for TJ migration, and the conditions of TJ migration are easily satisfied. TJ migration by this means implies that TJs may migrate rapidly at first by the primary modes and then accumulate stress and stagnate (barring the extremely rare/special case in which the primary disconnections can satisfy both conditions simultaneously), after which their migration is controlled by the formation of secondary disconnections.

At high temperature, when the population of secondary disconnections is larger, stagnation is easily overcome. This is consistent with the GB simulations in *TJ Migration Simulations*. However, the same simulations showed that GB migration may stagnate at low temperature; this is associated with the large energetic penalties associated with forming secondary-mode disconnections. This explains the TJ stagnation observed in the 800-K GB simulations.

As described above and seen in the polycrystal simulations (Figs. 1–3), stresses can be relaxed during microstructure evolution by dislocation and twin emission from GBs and TJs. If the TJ can emit dislocations along N distinct slip planes, then Eq. 6 becomes

$$\sum_{i=1}^3 J^{(i)} \mathbf{b}^{(i)} + \sum_{m=1}^N J^{L_m} \mathbf{b}^{L_m} = 0, \quad [8]$$

where J^{L_m} and \mathbf{b}^{L_m} denote fluxes and Burgers vectors of lattice dislocations, respectively. With the additional degrees of freedom provided by lattice dislocation flux, TJ migration may occur without new disconnection-mode activation. Likewise, sequential twinning at TJs may be a deformation process (89) that relaxes the accumulating internal stress.

Dislocation emission into the grains is a viable accommodation mechanism only if the slip planes in the crystal are suitably oriented to dissipate the accumulated Burgers vector. Coherent twin boundaries form on a restricted set of lattice planes and so may assist TJ migration only for particular lattice orientations and migration directions. This leaves secondary disconnection nucleation as the general determiner of TJ migration. In this framework, TJ mobility M_{TJ} is no longer an intrinsic property of a TJ, but rather must be determined directly in terms of disconnection types, densities, and mobilities. At low temperature, some TJs should be highly mobile while others are effectively sessile, depending on the availability of secondary disconnection modes. This disparity should vanish at high temperature where the formation of multiple disconnection types is likely. More fundamentally, this implies that through the disconnection mechanism, GB and TJ migrations are deeply intertwined and disconnection theory can yield a unified framework for microstructure evolution. In the next section, we build a continuum description of microstructure evolution accounting for GB and TJ migration within the context of disconnection motion.

Continuum Model

Zhang et al. (40) developed an equation of motion for the evolution of GB profiles based on a single disconnection-mode model. In this model, the disconnection density is a continuous variable and the dynamics account for both disconnection nucleation and migration. We extend this method to consider both multiple disconnection modes and disconnection-mediated TJ motion. The profile of $\text{GB}^{(i)}$ is described by $z^{(i)}$, which measures the GB “height” above some reference plane parallel to the symmetric GB; it evolves as

$$z_{,t}^{(i)} = - \sum_{j=1,2} v_j^{(i)} (|\rho_j^{(i)}| h_j^{(i)} + 2\eta_j^{(i)}), \quad [9]$$

where $z_{,t}^{(i)}$ denotes the derivative of $z^{(i)}$ with respect to time. $v_j^{(i)}$ is the glide velocity of j th-mode disconnections on $\text{GB}^{(i)}$ and is given by

$$v_j^{(i)} = M_d \left[(\boldsymbol{\sigma} + \boldsymbol{\tau}) \mathbf{b}_j^{(i)} + \Psi h_j^{(i)} - \gamma z_{,xx} h_j^{(i)} \right], \quad [10]$$

where M_d is a disconnection mobility, $\boldsymbol{\sigma}$ is the contribution to stress from other disconnections, and $\boldsymbol{\tau}$ is any external stress. The $(\boldsymbol{\sigma} + \boldsymbol{\tau}) \mathbf{b}_j^{(i)}$ term represents an appropriate summation over stress and Burgers vector components as in the Peach–Koehler force (90). In the limit that the GB is close to a symmetric inclination, such that $\mathbf{b}_j^{(i)}$ lies parallel to the GB plane, we can consider the shear stresses resolved along the GB plane σ and τ , as well as the scalar $b_j^{(i)} = |\mathbf{b}_j^{(i)}|$. Finally, the background thermal density of disconnections (scaled by step height) $\eta_j^{(i)}$ is

$$\eta_j^{(i)} = \frac{h_j^{(i)}}{a} e^{-E_j^{(i)}/(k_B T)}, \quad [11]$$

where a is an atomic spacing, and $E_j^{(i)}$ is half the disconnection pair formation energy (40).

We consider three grain boundaries $\text{GB}^{(1)}$, $\text{GB}^{(2)}$, and $\text{GB}^{(3)}$, which meet at a triple junction $P = \mathbf{x}_0$. We further assume that each $\text{GB}^{(i)}$ has two possible disconnection modes ($b_1^{(i)}$, $b_2^{(i)}$) and

($b_2^{(i)}$, $h_2^{(i)}$), such that $b_1^{(i)} b_2^{(i)} > 0$ and $h_1^{(i)} h_2^{(i)} < 0$ (β_1 and β_2 have opposite sign). The TJ migrates to reduce the total energy of the system via the exchange of disconnections between the TJ and its constituent GBs. TJ motion is therefore related to the step flux into/from the GB,

$$J_1^{(i)} h_1^{(i)} + J_2^{(i)} h_2^{(i)} = -\mathbf{v}_{\text{TJ}} \cdot \mathbf{n}^{(i)}, \quad [12]$$

where $J_j^{(i)}$ is the flux of j th-mode disconnections from the i th GB and $\mathbf{n}^{(i)}$ is the normal to the i th GB symmetric inclination. The Burgers vector flux into the TJ is then

$$\frac{d}{dt} \mathbf{b}_{\text{TJ}} = \sum_{i=1,2,3} J_1^{(i)} \mathbf{b}_1^{(i)} + J_2^{(i)} \mathbf{b}_2^{(i)}, \quad [13]$$

where \mathbf{b}_{TJ} is the total Burgers vector at the TJ.

The change in total energy due to TJ motion has contributions from both the disconnection step and the Burgers vector. When a net Burgers vector is present at the TJ, the TJ will tend to absorb nearby disconnections (or emit disconnections) to cancel this accumulated Burgers vector and reduce the $\|\mathbf{b}_{\text{TJ}}\|^2$ energy contribution. This cancellation happens very quickly and, in the continuum limit, we assume that the zero accumulated Burgers vector condition $\mathbf{b}_{\text{TJ}} = 0$ holds during TJ motion. Thus, the driving force on TJ motion is solely described by the variation of the energy associated with surface tension (from the disconnection step character and the GB energy itself),

$$\mathbf{v}_{\text{TJ}} = M_{\text{TJ}} \sum_{i=1,2,3} \gamma^{(i)} \mathbf{t}^{(i)}, \quad [14]$$

where M_{TJ} is the TJ mobility, $\gamma^{(i)}$ is the GB energy, and $\mathbf{t}^{(i)}$ is the unit vector tangent to $\text{GB}^{(i)}$. In particular, $\mathbf{v}_{\text{TJ}} = 0$ defines the equilibrium angles in Eq. 2. While this equation of motion merges with the classical continuum form of TJ motion, the TJ mobility is not an intrinsic (well-defined) property of the TJ. The TJ mobility is ultimately governed by the disconnection availability and mobility.

The problem of TJ migration reduces to the optimization problem (where $M_{\text{TJ}} \geq 0$)

$$\max |\mathbf{v}_{\text{TJ}}| = M_{\text{TJ}} \left\| \sum_{i=1,2,3} \gamma^{(i)} \mathbf{t}^{(i)} \right\|, \quad [15]$$

subject to constraints

$$\sum_i J_1^{(i)} \mathbf{b}_1^{(i)} + J_2^{(i)} \mathbf{b}_2^{(i)} = \mathbf{0} \quad [16]$$

$$J_1^{(i)} h_1^{(i)} + J_2^{(i)} h_2^{(i)} = -\mathbf{v}_{\text{TJ}} \cdot \mathbf{n}^{(i)} \quad [17]$$

$$|J_j^{(i)} h_j^{(i)}| \leq M_d \left| \eta_j^{(i)} \mathbf{n}^{(i)} \cdot \sum_{k=1,2,3} \gamma^{(k)} \mathbf{t}^{(k)} \right|, \quad [18]$$

where $i = \{1, 2, 3\}$ and $j = \{1, 2\}$. Eqs. 16 and 17 refer to the zero Burgers vector accumulation and zero displacement incompleteness conditions. The inequality Eq. 18 implies that not all nucleated (positive or negative) disconnections can contribute to TJ motion due to the above two constraints, where the right-hand side describes the maximal possible disconnection flux (scaled by step height). The driving force acting on a disconnection at the TJ is $\mathbf{n}^{(i)} \cdot \sum_{k=1,2,3} \gamma^{(k)} \mathbf{t}^{(k)}$, and the available disconnections are limited by the scaled thermal density $\eta_j^{(i)}$. Use of the maximal TJ velocity is consistent with the assumption that TJ motion is overdamped and occurs in the direction of the maximum force on the TJ.

1. Hillert M (1965) On the theory of normal and abnormal grain growth. *Acta Metallurgica* 13:227–238.
2. MacPherson RD, Srolovitz DJ (2007) The von Neumann relation generalized to coarsening of three-dimensional microstructures. *Nature* 446:1053–1055.
3. Sonnweber-Ribic P, Gruber PA, Dehm G, Strunk HP, Arzt E (2012) Kinetics and driving forces of abnormal grain growth in thin Cu films. *Acta Materialia* 60:2397–2406.
4. Herring C (1951) Surface tension as a motivation for sintering. *Phys Powder Metall* 27:143–179.
5. King AH (1999) The geometric and thermodynamic properties of grain boundary junctions. *Interf Sci* 7:251–271.
6. Grest G, Srolovitz D, Anderson M (1985) Computer simulation of grain growth—IV. Anisotropic grain boundary energies. *Acta Metallurgica* 33:509–520.
7. Abbruzzese G, Lücke K (1986) A theory of texture controlled grain growth—I. Derivation and general discussion of the model. *Acta Metallurgica* 34:905–914.
8. Holm EA, Hassold GN, Miodownik MA (2001) On misorientation distribution evolution during anisotropic grain growth. *Acta Materialia* 49:2981–2991.
9. Kazaryan A, Wang Y, Dregia S, Patton B (2002) Grain growth in anisotropic systems: Comparison of effects of energy and mobility. *Acta Materialia* 50:2491–2502.
10. Upmanyu M, et al. (2002) Boundary mobility and energy anisotropy effects on microstructural evolution during grain growth. *Interf Sci* 10:201–216.
11. Gruber J, George DC, Kuprat AP, Rohrer GS, Rollett AD (2005) Effect of anisotropic grain boundary properties on grain boundary plane distributions during grain growth. *Scripta Materialia* 53:351–355.
12. Moelans N, Blanpain B, Wollants P (2008) Quantitative analysis of grain boundary properties in a generalized phase field model for grain growth in anisotropic systems. *Phys Rev B* 78:024113.
13. Gottstein G, Sursaeva V, Shvindlerman LS (1999) The effect of triple junctions on grain boundary motion and grain microstructure evolution. *Interf Sci* 7:273–283.
14. Gottstein G, King A, Shvindlerman L (2000) The effect of triple-junction drag on grain growth. *Acta Materialia* 48:397–403.
15. Gottstein G, Shvindlerman LS (2002) Triple junction drag and grain growth in 2D polycrystals. *Acta Materialia* 50:703–713.
16. Protasova S, Gottstein G, Molodov D, Sursaeva V, Shvindlerman L (2001) Triple junction motion in aluminum tricrystals. *Acta Materialia* 49:2519–2525.
17. Mattissen D, Molodov D, Shvindlerman L, Gottstein G (2005) Drag effect of triple junctions on grain boundary and grain growth kinetics in aluminium. *Acta Materialia* 53:2049–2057.
18. Upmanyu M, Srolovitz D, Shvindlerman L, Gottstein G (1999) Triple junction mobility: A molecular dynamics study. *Interf Sci* 7:307–319.
19. Czubayko U, Sursaeva V, Gottstein G, Shvindlerman L (1998) Influence of triple junctions on grain boundary motion. *Acta Materialia* 46:5863–5871.
20. Gottstein G, Shvindlerman L, Zhao B (2010) Thermodynamics and kinetics of grain boundary triple junctions in metals: Recent developments. *Scripta Materialia* 62: 914–917.
21. Krill C, III, et al. (2001) Size-dependent grain-growth kinetics observed in nanocrystalline Fe. *Phys Rev Lett* 86:842–845.
22. Chokshi AH (2008) Triple junction limited grain growth in nanomaterials. *Scripta Materialia* 59:726–729.
23. Gleiter H (1969) The formation of annealing twins. *Acta Metallurgica* 17:1421–1428.
24. Hirth J, Balluffi R (1973) On grain boundary dislocations and ledges. *Acta Metallurgica* 21:929–942.
25. Rae C, Smith D (1980) On the mechanisms of grain boundary migration. *Philos Mag* A 41:477–492.
26. Balluffi R, Brokman A, King A (1982) CSL/DSC lattice model for general crystal-crystal boundaries and their line defects. *Acta Metallurgica* 30:1453–1470.
27. Hirth J, Pond R (1996) Steps, dislocations and disconnections as interface defects relating to structure and phase transformations. *Acta Materialia* 44:4749–4763.
28. Winning M, Gottstein G, Shvindlerman L (2002) On the mechanisms of grain boundary migration. *Acta Materialia* 50:353–363.
29. Cahn JW, Taylor JE (2004) A unified approach to motion of grain boundaries, relative tangential translation along grain boundaries, and grain rotation. *Acta Materialia* 52:4887–4898.
30. Cahn JW, Mishin Y, Suzuki A (2006) Coupling grain boundary motion to shear deformation. *Acta Materialia* 54:4953–4975.
31. Gorkaya T, Molodov DA, Gottstein G (2009) Stress-driven migration of symmetrical $\langle 1\ 0\ 0 \rangle$ tilt grain boundaries in Al bicrystals. *Acta Materialia* 57:5396–5405.
32. Sheikh-Ali A (2010) Coupling of grain boundary sliding and migration within the range of boundary specialness. *Acta Materialia* 58:6249–6255.
33. Wan L, Wang S (2010) Shear response of the $\sigma\ 9\ \langle 110 \rangle\ \{211\}$ symmetric tilt grain boundary in FCC metals studied by atomistic simulation methods. *Phys Rev B* 82:214112.
34. Karma A, Trautt ZT, Mishin Y (2012) Relationship between equilibrium fluctuations and shear-coupled motion of grain boundaries. *Phys Rev Lett* 109:095501.
35. Khater H, Serra A, Pond R, Hirth J (2012) The disconnection mechanism of coupled migration and shear at grain boundaries. *Acta Materialia* 60:2007–2020.
36. Rajabzadeh A, Mompou F, Legros M, Combe N (2013) Elementary mechanisms of shear-coupled grain boundary migration. *Phys Rev Lett* 110:265507.
37. Rajabzadeh A, Legros M, Combe N, Mompou F, Molodov D (2013) Evidence of grain boundary dislocation step motion associated to shear-coupled grain boundary migration. *Philos Mag* 93:1299–1316.
38. Han J, Thomas SL, Srolovitz DJ (2018) Grain-boundary kinetics: A unified approach. *Prog Mater Sci* 98:386–476.
39. Sun L, He X, Lu J (2018) Nanotwinned and hierarchical nanotwinned metals: A review of experimental, computational and theoretical efforts. *NPG Comput Mater* 4:6.
40. Zhang L, Han J, Xiang Y, Srolovitz DJ (2017) Equation of motion for a grain boundary. *Phys Rev Lett* 119:246101.
41. Li CH, Edwards EH, Washburn J, Parker ER (1953) Stress-induced movement of crystal boundaries. *Acta Metallurgica* 1:223–229.
42. Bainbridge DW, Choh HL, Edwards EH (1954) Recent observations on the motion of small angle dislocation boundaries. *Acta Metallurgica* 2:322–333.
43. Winning M, Gottstein G, Shvindlerman L (2001) Stress induced grain boundary motion. *Acta Materialia* 49:211–219.
44. Winning M, Gottstein G, Shvindlerman L (2001) Migration of grain boundaries under the influence of an external shear stress. *Mater Sci Eng A* 317:17–20.
45. Gottstein G, Molodov D, Shvindlerman L, Srolovitz D, Winning M (2001) Grain boundary migration: Misorientation dependence. *Curr Opin Solid State Mater Sci* 5:9–14.
46. Molteni C, Francis G, Payne M, Heine V (1996) First principles simulation of grain boundary sliding. *Phys Rev Lett* 76:1284–1287.
47. Molteni C, Francis O, Payne M, Heine V (1996) Grain boundary sliding: An *ab initio* simulation. *Mater Sci Eng B* 37:121–126.
48. Molteni C, Marzari N, Payne M, Heine V (1997) Sliding mechanisms in aluminum grain boundaries. *Phys Rev Lett* 79:869–872.
49. Hamilton J, Foiles S (2002) First-principles calculations of grain boundary theoretical shear strength using transition state finding to determine generalized gamma surface cross sections. *Phys Rev B* 65:064104.
50. Chen LQ, Kalonji G (1992) Finite temperature structure and properties of $\sigma = 5(310)$ tilt grain boundaries in NaCl a molecular dynamics study. *Philos Mag* A 66:11–26.
51. Shiga M, Shinoda W (2004) Stress-assisted grain boundary sliding and migration at finite temperature: A molecular dynamics study. *Phys Rev B* 70:054102.
52. Sansoz F, Molinari J (2005) Mechanical behavior of σ tilt grain boundaries in nanoscale Cu and Al: A quasicontinuum study. *Acta Materialia* 53:1931–1944.
53. Trautt Z, Adland A, Karma A, Mishin Y (2012) Coupled motion of asymmetrical tilt grain boundaries: Molecular dynamics and phase field crystal simulations. *Acta Materialia* 60:6528–6546.
54. Homer ER, Foiles SM, Holm EA, Olmsted DL (2013) Phenomenology of shear-coupled grain boundary motion in symmetric tilt and general grain boundaries. *Acta Materialia* 61:1048–1060.
55. Rajabzadeh A, et al. (2014) The role of disconnections in deformation-coupled grain boundary migration. *Acta Materialia* 77:223–235.
56. Mompou F, Legros M, Ensslen C, Kraft O (2015) In situ TEM study of twin boundary migration in sub-micron Be fibers. *Acta Materialia* 96:57–65.
57. Pond R, Smith D, Southerden P (1978) On the role of grain boundary dislocations in high temperature creep. *Philos Mag* A 37:27–40.
58. Guillope M, Poirier J (1980) A model for stress-induced migration of tilt grain boundaries in crystals of NaCl structure. *Acta Metallurgica* 28:163–167.
59. Bishop GH, Jr, Harrison RJ, Kwok T, Yip S (1982) Computer molecular-dynamics studies of grain-boundary structures. I. Observations of coupled sliding and migration in a three-dimensional simulation. *J Appl Phys* 53:5596–5608.
60. Hirth J (1994) Dislocations, steps and disconnections at interfaces. *J Phys Chem Sol* 55:985–989.
61. Hyde B, Farkas D, Caturla M (2005) Atomistic sliding mechanisms of the $\sigma = 5$ symmetric tilt grain boundary in BCC iron. *Philos Mag* 85:3795–3807.
62. Bollmann W (1970) General geometrical theory of crystalline interfaces. *Crystal Defects and Crystalline Interfaces* (Springer, Berlin), pp 143–185.
63. Ashby M (1972) Boundary defects, and atomistic aspects of boundary sliding and diffusional creep. *Surf Sci* 31:498–542.
64. King AH, Smith D (1980) The effects on grain-boundary processes of the steps in the boundary plane associated with the cores of grain-boundary dislocations. *Acta Cryst* A 36:335–343.
65. Thomas SL, Chen K, Han J, Purohit PK, Srolovitz DJ (2017) Reconciling grain growth and shear-coupled grain boundary migration. *Nat Commun* 8:1764.
66. Sisanbaev A, Valiev R (1992) The effect of triple junction type on grain-boundary sliding and accommodation in aluminium tricrystals. *Acta Metallurgica Materialia* 40:3349–3356.
67. Hashimoto S, Fujii T, Miura S (1987) Grain-boundary sliding and triple-point fold in aluminum tricrystals. *Scripta Metallurgica* 21:169–174.
68. Chen M, et al. (2003) Deformation twinning in nanocrystalline aluminum. *Science* 300:1275–1277.
69. Liao X, et al. (2003) Deformation mechanism in nanocrystalline Al: Partial dislocation slip. *Appl Phys Lett* 83:632–634.
70. Van Swygenhoven H, Derlet P, Hasnaoui A (2002) Atomic mechanism for dislocation emission from nanosized grain boundaries. *Phys Rev B* 66:024101.
71. Van Swygenhoven H, Derlet PM (2001) Grain-boundary sliding in nanocrystalline FCC metals. *Phys Rev B* 64:224105.
72. Mason JK, Lazar EA, MacPherson RD, Srolovitz DJ (2015) Geometric and topological properties of the canonical grain-growth microstructure. *Phys Rev E* 92: 063308.
73. Thomas SL, King AH, Srolovitz DJ (2016) When twins collide: Twin junctions in nanocrystalline nickel. *Acta Materialia* 113:301–310.
74. Lin B, et al. (2015) Observation of annealing twin nucleation at triple lines in nickel during grain growth. *Acta Materialia* 99:63–68.
75. Fullman RL, Fisher JC (1951) Formation of annealing twins during grain growth. *J Appl Phys* 22:1350–1355.
76. Burgers W, Meijis J, Tiedema T (1953) Frequency of annealing twins in copper crystals grown by recrystallization. *Acta Metallurgica* 1:75–78.
77. Dash S, Brown N (1963) An investigation of the origin and growth of annealing twins. *Acta Metallurgica* 11:1067–1075.

78. Mahajan S, Pande C, Imam M, Rath B (1997) Formation of annealing twins in FCC crystals. *Acta Materialia* 45:2633–2638.
79. Farkas D, Bringa E, Caro A (2007) Annealing twins in nanocrystalline FCC metals: A molecular dynamics simulation. *Phys Rev B* 75:184111.
80. Jin Y, et al. (2014) Annealing twin development during recrystallization and grain growth in pure nickel. *Mater Sci Eng A* 597:295–303.
81. Faken D, Jónsson H (1994) Systematic analysis of local atomic structure combined with 3D computer graphics. *Comput Mater Sci* 2:279–286.
82. Stukowski A (2010) Visualization and analysis of atomistic simulation data with OVITO—The open visualization tool. *Model Simulation Mater Sci Eng* 18:015012.
83. Kelchner CL, Plimpton S, Hamilton J (1998) Dislocation nucleation and defect structure during surface indentation. *Phys Rev B* 58:11085–11088.
84. Mishin Y, Farkas D, Mehl MJ, Papaconstantopoulos DA (1999) Interatomic potentials for monoatomic metals from experimental data and *ab initio* calculations. *Phys Rev B* 59:3393–3407.
85. Lazar EA, Mason JK, MacPherson RD, Srolovitz DJ (2011) A more accurate three-dimensional grain growth algorithm. *Acta Materialia* 59:6837–6847.
86. Hunter A, Beyerlein I (2014) Predictions of an alternative pathway for grain-boundary driven twinning. *Appl Phys Lett* 104:233112.
87. Upmanyu M, Srolovitz D, Shvindlerman L, Gottstein G (2002) Molecular dynamics simulation of triple junction migration. *Acta Materialia* 50:1405–1420.
88. Combe N, Momprou F, Legros M (2016) Disconnections kinks and competing modes in shear-coupled grain boundary migration. *Phys Rev B* 93:024109.
89. Christian JW, Mahajan S (1995) Deformation twinning. *Prog Mater Sci* 39: 1–157.
90. Peach M, Koehler J (1950) The forces exerted on dislocations and the stress fields produced by them. *Phys Rev* 80:436–439.
91. Holm EA, Foiles SM (2010) How grain growth stops: A mechanism for grain-growth stagnation in pure materials. *Science* 328:1138–1141.
92. Einstein A (2010) *The Ultimate Quotable Einstein* (Princeton Univ Press, Princeton).